

Optics Letters

Multifocal metalens based on multilayer Pancharatnam–Berry phase elements architecture

RONGHUI LIN  AND XIAOHANG LI* 

King Abdullah University of Science and Technology (KAUST), Advanced Semiconductor Laboratory, Thuwal 23955-6900, Saudi Arabia

*Corresponding author: xiaohang.li@kaust.edu.sa

Received 1 April 2019; revised 3 May 2019; accepted 3 May 2019; posted 6 May 2019 (Doc. ID 363827); published 28 May 2019

In this Letter, we aim to answer the fundamental question of what will happen when two layers of Pancharatnam–Berry phase elements are superimposed on each other. The different diffraction orders and their respective phase changes of this structure are investigated by Jones matrix calculations. Based on the results, we propose and demonstrate metalenses numerically that can split an incident circularly polarized beam into different helicities and focus them at different foci with controlled intensity and focal length. The decoupling of the focusing length and the relative intensity give us control to achieve an arbitrary combination of focal spot location and relative intensity. To the best of our knowledge, this is the first proposal and theoretical demonstration of bilayer Pancharatnam–Berry phase elements for metalens applications. Such a platform can be expanded to multilayers and applied to other complex functionalities such as achromatic lenses. © 2019 Optical Society of America

<https://doi.org/10.1364/OL.44.002819>

Metasurfaces have drawn considerable attention in recent years due to their versatile wavefront shaping capabilities, ultrathin geometries, and batch production possibilities [1]. It is a promising technology to replace conventional bulky and expensive lenses, especially in portable and wearable devices. Enormous efforts have been devoted to develop various optical devices using this technology, such as focusing lenses [2], axicons [3], optical orbital angular momentum generation [4], and holograms [5]. However, more complicated functionalities often require a more complex design. One common way of expanding the design parameter space is to use spatial multiplexing schemes [6]. However, multiplexing interrupts the phase smoothness, thus bringing undesirable diffractive orders and reduced performance [1,7]. Also, the intrinsic space-filling limitation is a problem for spatial multiplexing.

Multilayer metalenses have been proposed to circumvent these restrictions. The idea is to extend the design parameter space into three dimensions. Therefore, an extra degree of freedom can be added, bringing more flexibility and versatility to the metalens design. Devices such as achromatic metalenses [7,8], zoom lens systems for imaging [9], and other advanced functionalities with improved efficiencies [10] have been

reported. However, the interlayer spacing is mostly large and less controllable. By taking advantage of the current nanofabrication capabilities, it is possible to make the two layers closer and more compact with increased alignment accuracy [8].

Metasurface design relies on the manipulation of local phase with subwavelength features. One way to achieve this is the Pancharatnam–Berry (P-B) phase, which can be imparted by the rotation of the nanofin elements [11]. Metalenses based on the P-B phase are easy to design, robust to fabrication errors, and intrinsically broadband [12]. Therefore, they are widely used in the design of various optical components for circular polarizations [13]. Despite the wide popularity of single-layer P-B phase optical components, bilayer and multilayer P-B phase metalenses have not yet been studied.

Bifocal and multifocal lenses allowing the incoming light to be focused at different focal spots can be applied in imaging [6], optical communication [14], and medical applications [15]. A straightforward way to achieve multifocal lenses is spatial multiplexing [6]. However, only part of the aperture contributes to the formation of each focal point, resulting in reduced focusing performance and difficulty in relative intensity control [16]. The multifocal lens can also be achieved by designing building blocks to utilize the combination of the propagation phase and P-B phase [16]. But this method requires a large library of building blocks to meet the requirements of P-B phase and propagation phase simultaneously. Thus, the designing procedure is challenging. In this study, we aim to solve the problems of multifocal lens design by using multilayer P-B phase architecture. First, we will answer the fundamental question of what will happen when two layers of P-B phase elements are superimposed on each other. When two layers of periodic structures are superimposed on top of each other, a third pattern with different periodicity can be perceived, which is called the Moiré effect [17]. Here, we theoretically show that a similar phenomenon can happen with two layers of P-B phase elements: a diffraction order with a phase shift equal to the rotation angle difference of the two layers can be observed. Based on theoretical calculations, we demonstrate that a multilayer metalens with arbitrary control of focal spot location and relative intensity can be achieved by multilayer P-B phase architecture.

Considering an anisotropic nanofin structure with the ordinary and extraordinary axes (o and e) shown in Fig. 1(a), the complex transmission coefficients of light with linear polarization

along the ordinary and extraordinary axes are denoted as t_o and t_e , respectively. As the nanofin is rotated by an angle of θ with respect to the laboratory axes (x and y), the transmission coefficients can be obtained by the following Jones matrix formalism [12]:

$$J(\theta)_{\text{linear}} = \begin{bmatrix} t_o \cos^2 \theta + t_e \sin^2 \theta & (t_o - t_e) \cos \theta \sin \theta \\ (t_o - t_e) \cos \theta \sin \theta & t_o \sin^2 \theta + t_e \cos^2 \theta \end{bmatrix}. \quad (1)$$

For simplicity and clarity, we work on circular polarization basis, and thereby we change from the linear basis \hat{x}, \hat{y} to the circular basis \hat{L}, \hat{R} using the following transformation: ($\hat{L} = \frac{\hat{x} + i\hat{y}}{\sqrt{2}}, \hat{R} = \frac{\hat{x} - i\hat{y}}{\sqrt{2}}$). The Jones matrix on the basis of circular polarization can be written as [18]

$$J(\theta)_{\text{circular}} = \begin{bmatrix} \frac{1}{2}(t_o + t_e) & \frac{1}{2}(t_o - t_e)e^{i2\theta} \\ \frac{1}{2}(t_o - t_e)e^{-j2\theta} & \frac{1}{2}(t_o + t_e) \end{bmatrix}. \quad (2)$$

Now if there are two layers of the P-B phase elements overlaying each other, the combined Jones matrix can be calculated as follows assuming their rotation angles are θ_1, θ_2 and the complex transmission coefficients are t_o, t_e, t'_o , and t'_e , respectively:

$$\begin{aligned} J(\theta_1, \theta_2) &= J(\theta_2)J(\theta_1) \\ &= \begin{bmatrix} \frac{1}{2}(t'_o + t'_e) & \frac{1}{2}(t'_o - t'_e)e^{i2\theta_2} \\ \frac{1}{2}(t'_o - t'_e)e^{-j2\theta_2} & \frac{1}{2}(t'_o + t'_e) \end{bmatrix} \begin{bmatrix} \frac{1}{2}(t_o + t_e) & \frac{1}{2}(t_o - t_e)e^{i2\theta_1} \\ \frac{1}{2}(t_o - t_e)e^{-j2\theta_1} & \frac{1}{2}(t_o + t_e) \end{bmatrix}. \end{aligned} \quad (3)$$

For simplicity, we will use the following notation:

$$\begin{cases} t_o + t_e = T_1, & t_o - t_e = T_2 \\ t'_o + t'_e = T'_1, & t'_o - t'_e = T'_2 \end{cases}. \quad (4)$$

After linear calculations, the Jones matrix of the system becomes

$$\begin{aligned} J(\theta_1, \theta_2)_{\text{combined}} &= \begin{bmatrix} \frac{1}{4}T_1T'_1 + \frac{1}{4}T_2T'_2e^{i2(\theta_2 - \theta_1)} & \frac{1}{4}T_2T'_1e^{i2\theta_1} + \frac{1}{4}T_1T'_2e^{i2\theta_2} \\ \frac{1}{4}T_2T'_1e^{-j2\theta_1} + \frac{1}{4}T_1T'_2e^{-j2\theta_2} & \frac{1}{4}T_1T'_1 + \frac{1}{4}T_2T'_2e^{i2(\theta_1 - \theta_2)} \end{bmatrix}. \end{aligned} \quad (5)$$

For right-handed circularly polarized (RCP) input ($\begin{smallmatrix} 1 \\ 0 \end{smallmatrix}$) passing through the system, the resultant transmitted light can be expressed as

$$\begin{aligned} E_t &= \frac{1}{4}T_1T'_1 \begin{pmatrix} 1 \\ 0 \end{pmatrix} + \frac{1}{4}T_2T'_2e^{i2(\theta_2 - \theta_1)} \begin{pmatrix} 1 \\ 0 \end{pmatrix} \\ &+ \frac{1}{4}T_2T'_1e^{-j2\theta_1} \begin{pmatrix} 0 \\ 1 \end{pmatrix} + \frac{1}{4}T_1T'_2e^{-j2\theta_2} \begin{pmatrix} 0 \\ 1 \end{pmatrix}. \end{aligned} \quad (6)$$

It contains four diffraction orders: the first order has the same helicity and phase as the incident light; the second one has the same helicity as the incident light, but it undergoes a phase change of $2(\theta_2 - \theta_1)$; the last two orders have helicity opposite to the incident light and experience a phase shift of $-2\theta_1$ and $-2\theta_2$, respectively. In theory, a metalens with three focusing points can be designed by utilizing these phase changes. However, the arbitrary control of three focal points is not possible with only two degrees of freedom θ_1 and θ_2 . So we focus our design on bifocal lenses, for which we set $T'_1 = 0$, and the output beam becomes

$$E_t = \frac{1}{4}T_2T'_2e^{i2(\theta_2 - \theta_1)} \begin{pmatrix} 1 \\ 0 \end{pmatrix} + \frac{1}{4}T_1T'_2e^{-j2\theta_2} \begin{pmatrix} 0 \\ 1 \end{pmatrix}. \quad (7)$$

The output beam consists of an RCP component with $2(\theta_2 - \theta_1)$ phase shift and a left-hand circularly polarized (LCP) component (cross polarization) with a phase shift of $-2\theta_2$. In order for these two diffraction orders to focus, the spatial variation of the phase shift has to meet the following condition:

$$\varphi_F(x, y) = \frac{2\pi}{\lambda} \left(F - \sqrt{x^2 + y^2 + F^2} \right), \quad (8)$$

where λ is the design wavelength, F is the focal length, and x and y represent the discretized spatial coordinates. The phase changes of the two diffraction orders have to meet the condition in Eq. (8) simultaneously:

$$\begin{cases} 2(\theta_2 - \theta_1) = \varphi_{F1}(x, y) \\ -2\theta_2 = \varphi_{F2}(x, y) \end{cases}. \quad (9)$$

By solving this simple equation, the spatially dependent rotation angles of each element can be obtained. The proposed metalens takes an input of RCP light and splits it into LCP and RCP components, which are focused at different focal spots F1 and F2, as illustrated in Fig. 1(c).

To materialize the bifocal function, we propose the structure shown in Fig. 1(d). Elliptical nanofin elements are chosen to account for the round corners that may occur during actual nanofabrication. Such a structure can be fabricated using current nanofabrication capabilities as follows [8]: first, a layer of TiO_2 P-B elements is deposited and fabricated on the substrate, on top of which a layer of filling material SiO_2 is deposited. After that, the second TiO_2 P-B elements layer is deposited and fabricated. The processing of both the first and second P-B phase elements layers is the same as reported in the literature [19]. The only difference is a filling material to facilitate the fabrication of the second P-B phase elements layer. In this study, SiO_2 and TiO_2 are used because they are widely adopted materials for metalens fabrication. Moreover, the refractive indices at the designed wavelength of these materials are 1.46 and 2.49, respectively, which gives us a reasonable index contrast for the first P-B elements layer.

To meet the condition $T'_1 = 0$, the geometrical parameters of the second P-B phase layer have to be optimized so that $|t_o| = |t_e|$ and $\arg(t_o) - \arg(t_e) = \pi$. A parameter sweep for the geometries of the second nanofin elements layer is carried out using the commercial three-dimensional (3D) finite-difference time-domain (FDTD) solver (FDTD solutions, Lumerical Inc). The periodicity, length d_2 , and height

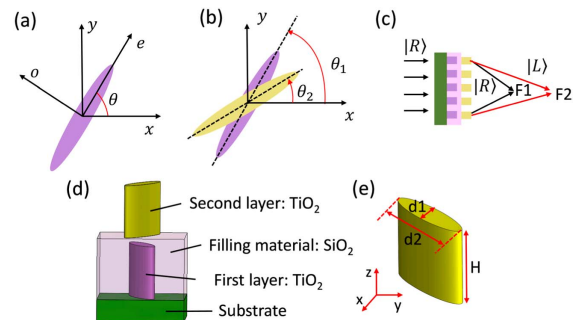


Fig. 1. (a) Rotation of the P-B elements, where o and e are the ordinary and extraordinary axes, respectively, and x and y are the laboratory axes. (b) Schematic showing the two rotation angles used in this study. (c) Illustration of the working principle of the proposed bifocal lens. (d) Schematic of the proposed structure. (e) Geometrical parameters that define a single P-B phase element.

of the nanofin H are set to be 300 nm, 200 nm, and 600 nm, respectively, while the width d_1 of the nanofin is varied to obtain the optimal value. Our designed wavelength is 480 nm, which lies in the visible spectrum.

To follow the conventions, we use transverse electric (TE) to represent the polarization state along the ordinary axis o , while the transverse magnetic (TM) represents the polarization state along the extraordinary axis e . Figure 2(a) shows the phase difference of TE and TM polarizations when the d_1 of the nanofin is 94 nm. For TE polarization, the phase of the transmitted field decreases in a smooth manner as the wavelength increases. In contrast, the phase of TM polarization shows three jumps in the spectrum at ~ 410 nm, ~ 460 nm, and ~ 505 nm, which corresponds to three TM resonances of the structure, as can be verified from the transmission curve [Fig. 2(b)] where a sudden drop of transmission is observed. These jumps can increase the phase difference (TM–TE), and therefore a phase difference of π at our designed wavelength of 480 nm is obtained. As shown in Fig. 2(b), the transmission of TM and TE polarizations at the designed wavelength of 480 nm are 0.86 and 0.89, respectively. In reality, it is difficult to find a geometry with identical TM and TE transmission while meeting the phase condition at the same time. However, the transmission is close enough to bring us satisfactory results, as shown in the following sections. Figure 2(c) shows the phase profile for both TE and TM polarizations at 480 nm with the optimized geometrical properties. The phase difference for TM and TE polarizations is exactly half a wavelength, which not only reduces the transmission into two terms as shown in Eq. (7) but also ensures a high polarization conversion efficiency of the second P-B elements layer. It is noted that nanofabrication errors are inevitable, leading to suboptimal geometries that may result in deteriorated efficiency and a third focal point at a distance corresponding to the phase shift of $-\theta_1$. However, a sweep of d_1 and d_2 within ± 20 nm of the optimized value reveals that the intensity of the third focal spot is much weaker than those of the main peaks.

Based on the optimized geometrical parameters and the rotation angles from Eq. (9), we build a 3D FDTD simulation model with an aperture size of $13 \mu\text{m} \times 13 \mu\text{m}$. The size of the whole simulation region is $14 \mu\text{m} \times 14 \mu\text{m} \times 22 \mu\text{m}$ with a mesh size of $10 \text{ nm} \times 10 \text{ nm} \times 20 \text{ nm}$ in the metalens region and $40 \text{ nm} \times 40 \text{ nm} \times 40 \text{ nm}$ in free space. The geometries of the first layer elements are the same as the second layer except the height is reduced to 400 nm to reduce the difficulty of the filling material deposition process. Three bifocal metalenses with different focal lengths are simulated.

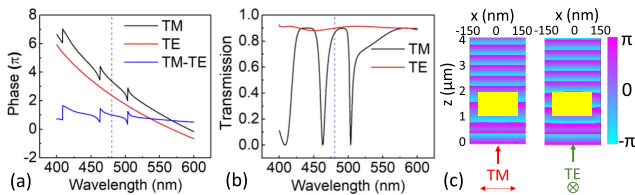


Fig. 2. Optimization of the second layer P-B phase elements. (a) Phase difference between TM and TE polarizations. (b) Transmission coefficient for TM and TE polarizations. (c) Simulated phase profile for TE and TM polarizations. The dashed lines in (a) and (b) represent the design wavelength 480 nm. The yellow block in (c) represents the P-B phase element.

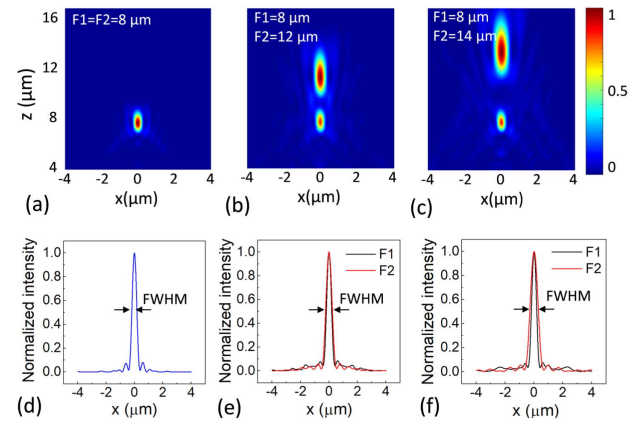


Fig. 3. (a)–(c) Electric field intensity profile for different design focal lengths. (a) Design 1: $F_1 = F_2 = 8 \mu\text{m}$, (b) design 2: $F_1 = 8 \mu\text{m}$, $F_2 = 12 \mu\text{m}$, and (c) design 3: $F_1 = 8 \mu\text{m}$, $F_2 = 14 \mu\text{m}$. (d)–(f) Intensity at the focal length in the lateral direction for different focal designs. (d) $F_1 = F_2 = 8 \mu\text{m}$, (e) $F_1 = 8 \mu\text{m}$, $F_2 = 12 \mu\text{m}$, and (f) $F_1 = 8 \mu\text{m}$, $F_2 = 14 \mu\text{m}$.

Figures 3(a)–3(c) show the electric field intensity profiles at the xz plane for different designs. In these designs, F_1 is fixed at $8 \mu\text{m}$, while F_2 is increased gradually. Clear focusing effects can be observed with minimal crosstalk between the focal spots. The intensity of the electric field at the focal length along the x direction is plotted in Figs. 3(d)–3(f), where the full-widths at half-maximum (FWHMs) of all the focal spots are close to the theoretical diffraction limited value of $\frac{\lambda}{2\text{NA}}$, with NA being the numerical aperture. The focusing properties are summarized in detail in Table 1. The simulated focal lengths are in good agreement with the designed values, despite some minor errors. As an example, we will analyze the focusing performance of design 2. With a lateral length of $13 \mu\text{m}$, the corresponding NAs of these two focal points are 0.65 and 0.5, which gives us diffraction-limited FWHMs of 369 nm and 488 nm, respectively. The FWHMs obtained from numerical simulations are 394 nm and 512 nm, which is close to the theoretical diffraction limit. Due to the computational restrictions in our case, we are unable to calculate a larger lens, so the NA of F_1 is much larger than that of F_2 . That explains why the focusing property of F_1 is better than F_2 [20]. In reality, this problem can be tackled by manufacturing a larger lens, and hence the NAs of both focal points are similar.

One advantage of the proposed architecture is its robust and straightforward design protocol. In the multifocal schemes that

Table 1. Focusing Performance of the Multifocal Metalens

		Designed Value (μm)	Simulated Value (μm)	FWHM (nm)	NA
Design 1	F_1	8	7.6	396	0.65
	F_2	8	7.6	396	0.65
Design 2	F_1	8	7.6	394	0.65
	F_2	12	11.5	512	0.5
Design 3	F_1	8	7.6	394	0.65
	F_2	14	13.3	570	0.44

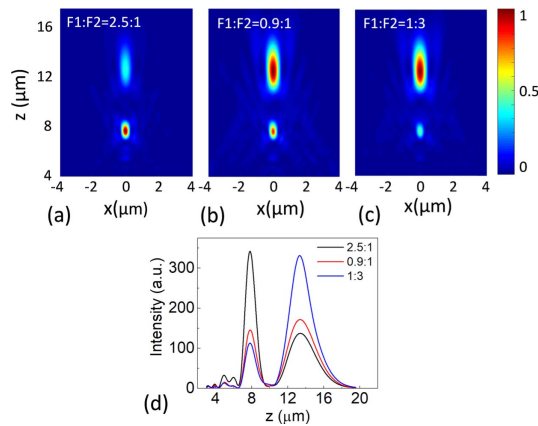


Fig. 4. (a)–(c) Electric field intensity profile for different design focal length ratios. (a) $F1:F2 = 2.5:1$, (b) $F1:F2 = 0.9:1$, and (c) $F1:F2 = 1:3$. (d) FWHM at the focal length in the longitudinal direction for different focal ratio designs.

rely on the combination of the propagation phase and P-B phase [16], both the propagation phase and TM–TE phase difference are controlled by the same set of geometrical parameters. A large amount of sweeping and optimization needs to be carried out to build up a library. In contrast, the design process is greatly simplified in the proposed architecture, since identical elements are used, and only one parameter sweeping is required to achieve the optimized geometry.

Another important factor to consider when designing multifocal lenses is the intensity ratios at the focal points. The intensity ratio of transmitted LCP and RCP light can be calculated from Eq. (7):

$$\frac{I_{F1}}{I_{F2}} = \frac{|T_2 T_2'|^2}{|T_1 T_1'|^2} = \frac{|T_2|^2}{|T_1|^2} = \frac{|t_o - t_e|^2}{|t_o + t_e|^2}. \quad (10)$$

The relative intensities at F1 and F2 are controlled solely by the t_o and t_e of the first layer. This property gives us the decoupling of focal spots position and relative intensity so arbitrary combinations of focal lengths and intensity ratios can be achieved. Figure 4 shows the electric field intensity profile of different ratios when the focal lengths are fixed. Different ratios are realized by adjusting the d1 of the first layer P-B phase elements while keeping the rotational angles and all other geometrical parameters fixed. Here, $\frac{I_{F1}}{I_{F2}}$ is calculated to be 2.5:1, 0.9:1, and 1:3 for three designs. Other ratios can also be obtained by changing the geometries of the first layer. A typical spatial multiplex scheme for multifocal metalenses is to divide the surface area into several concentric rings [6]. Each ring corresponds to one focal spot. Since only part of the aperture is involved in the formation of each focal spot, the focusing efficiency and NA corresponding to each ring can be quite different, which makes the relative intensity more difficult to control. Compared to this method, identical nanofins are used in this study all across the lens surface, and the relative intensity depends only on transmission of the first layer. Moreover, the whole surface is involved in the formation of each focal spot, and the NA varies in a controllable manner. Thus, it is a straightforward and robust way of designing multifocal lenses. Furthermore, the number of layers can be increased by taking advantage of nanofabrication technology, giving us

more parameters to achieve more complicated functionalities, such as multifocal lenses and achromatic lenses.

In conclusion, we propose a multilayer P-B phase metalens architecture and study the bilayer architecture in detail. Theoretical analysis shows the output beam has four orders of polarization: one maintains the input helicity and phase; another one maintains the input helicity but assumes a phase change of $2(\theta_2 - \theta_1)$; the last two orders of diffraction have the opposite helicity and experience a phase shift of $-2\theta_1$ and $-2\theta_2$, respectively. Based on these calculations, we design a bifocal metalens system with separate control of focal position and relative intensity that has not yet been realized in reported bifocal metalens systems. It is a straightforward and robust way to achieve bifocal metalenses. Such architecture can be extended to multilayers and be employed to achieve more complicated functionalities.

Funding. King Abdullah University of Science and Technology (KAUST) (Baseline Funds BAS/1/1664-01-01, Competitive Research Grants URF/1/3437-01-01, Competitive Research Grants URF/1/3771-01-01); Global Collaborative Research, King Abdullah University of Science and Technology (GCR, KAUST) (REP/1/3189-01-01).

Acknowledgment. The authors would like to thank Professor Enzo Di Fabrizio for sharing with us the Lumerical FDTD Solutions software.

REFERENCES

1. M. Khorasaninejad and F. Capasso, *Science* **358**, 1 (2017).
2. W. T. Chen, A. Y. Zhu, V. Sanjeev, M. Khorasaninejad, Z. J. Shi, E. Lee, and F. Capasso, *Nat. Nanotechnol.* **13**, 220 (2018).
3. W. T. Chen, M. Khorasaninejad, A. Y. Zhu, J. Oh, R. C. Devlin, A. Zaidi, and F. Capasso, *Light: Sci. Appl.* **6**, e16259 (2017).
4. E. Karimi, S. A. Schulz, I. De Leon, H. Qassim, J. Upham, and R. W. Boyd, *Light: Sci. Appl.* **3**, e167 (2014).
5. L. L. Li, T. J. Cui, W. Ji, S. Liu, J. Ding, X. Wan, Y. B. Li, M. H. Jiang, C. W. Qiu, and S. Zhang, *Nat. Commun.* **8**, 197 (2017).
6. X. Z. Chen, M. Chen, M. Q. Mehmood, D. D. Wen, F. Y. Yue, C. W. Qiu, and S. Zhang, *Adv. Opt. Mater.* **3**, 1201 (2015).
7. Y. Zhou, I. I. Kravchenko, H. Wang, J. R. Nolen, G. Gu, and J. Valentine, *Nano Lett.* **18**, 7529 (2018).
8. O. Avayu, E. Almeida, Y. Prior, and T. Ellenbogen, *Nat. Commun.* **8**, 14992 (2017).
9. G. X. Zheng, W. B. A. Wu, Z. L. Li, S. Zhang, M. Q. Mehmood, P. A. He, and S. Li, *Opt. Lett.* **42**, 1261 (2017).
10. F. Qin, L. Ding, L. Zhang, F. Monticone, C. C. Chum, J. Deng, S. T. Mei, Y. Li, J. H. Teng, M. H. Hong, S. Zhang, A. Alu, and C. W. Qiu, *Sci. Adv.* **2** (2016).
11. Z. Bomzon, V. Kleiner, and E. Hasman, *Opt. Lett.* **26**, 1424 (2001).
12. H.-H. Hsiao, C. H. Chu, and D. P. Tsai, *Small Methods* **1**, 1600064 (2017).
13. D. M. Lin, P. Y. Fan, E. Hasman, and M. L. Brongersma, *Science* **345**, 298 (2014).
14. J. W. He, J. S. Ye, X. K. Wang, Q. Kan, and Y. Zhang, *Sci. Rep.* **6**, 28800 (2016).
15. P. de Gracia, C. Dorronsoro, and S. Marcos, *Opt. Lett.* **38**, 3526 (2013).
16. S. N. Tian, H. M. Guo, J. B. Hu, and S. L. Zhuang, *Opt. Express* **27**, 680 (2019).
17. V. Saveljev, S.-K. Kim, and J. Kim, *Opt. Eng.* **57**, 1 (2018).
18. M. Kang, T. H. Feng, H.-T. Wang, and J. S. Li, *Opt. Express* **20**, 15882 (2012).
19. M. Khorasaninejad, W. T. Chen, A. Y. Zhu, J. Oh, R. C. Devlin, C. Roques-Carnes, I. Mishra, and F. Capasso, *IEEE J. Sel. Top. Quantum* **23**, 4700216 (2017).
20. H. Yang, G. H. Li, X. F. Su, G. T. Cao, Z. Y. Zhao, X. S. Chen, and W. Lu, *Sci. Rep.* **7**, 12632 (2017).